Chapter 5
Liquid Interface Self-Assembly of Colloidal Nanoplatelets for Optoelectronics

Abstract In this chapter, we discuss how liquid interface self-assembly can contribute to the utilization of colloidal semiconductor nanoplatelets in optoelectronics. Self-assembled nanoplatelet mono- or multilayers can be used as two-dimensional optically active waveguides, gain media of ultra-thin lasers, or energy transfer-based photosensitizers.

Keywords Optoelectronics · Nonradiative energy transfer · Optical gain · Waveguides · Photosensitization

The previous reports summarized in Table 4.1 not only propose various approaches for liquid interface self-assembly of colloidal nanoplatelets (NPLs) but also discuss and study the potential uses of these self-assembled NPLs for different optoelectronic applications. As argued earlier, anisotropy in optical and electronic properties of NPLs can be highly useful in enhancing the performance of optoelectronic devices employing colloidal nanocrystals (NCs). Liquid interface NPL assembly can, therefore, serve as a tool to exploit this NPL anisotropy and benefit the devices in which these NPLs are employed. The bottom-up approach of NPL deposition also facilitates the construction of NPL superlattices at desired film thickness.

5.1 Orientation-Controlled Nonradiative Energy Transfer with Self-Assembled Nanoplatelet Monolayers

Part of this section is adapted with permission from [1]. Copyright 2019 American Chemical Society.

The phenomenon of nonradiative migration of excitation energy from one fluorophore (donor) to another one (acceptor) in the close proximity is known as Förster (or fluorescence) resonance energy transfer (FRET). Named after Theodore Förster, who was the first to come up with an accurate theoretical description of the phenomenon [2], FRET is induced by near-field oscillating dipole interactions

O. Erdem and H. V. Demir, *Oriented Self-Assembly of Colloidal Semiconductor Nanoplatelets on Liquid Interfaces*, Nanoscience and Nanotechnology,
https://doi.org/10.1007/978-981-19-7052-8_5

between the donor and acceptor fluorophores. FRET is significantly distance sensitive for most donor–acceptor pairs and can occur only when the donor and acceptor are close (10 nm or less). FRET can also be referred to as nonradiative energy transfer (NRET), as no photon is emitted during the excitonic energy migration through FRET.

Initially, FRET has been extensively studied with fluorescent organic dyes or proteins and employed in their biological applications such as distance measurement, biosensing, and fluorescence microscopy [3–7]. The prospects of FRET using colloidal NCs have gained attraction due to the high absorption cross-section and spectral tunability of semiconductor NCs, which is a favorable property for high-efficiency energy transfer [8–10].

Apart from the distance between the donor and the acceptor, the strength of FRET depends on the presence of the resonant states in the two fluorophores, the refractive index of the medium, and the relative orientation of the dipole states of the donor and acceptor. In the most straightforward case of two pointlike dipoles representing donor and acceptor in a homogeneous medium, the rate of nonradiative energy transfer is given by

$$k_T = \frac{\kappa^2}{r^6 \cdot \tau} \frac{9 \ln 10}{128\pi^5 N n^4} J_\lambda \tag{5.1}$$

where r is the donor–acceptor distance, N is Avogadro's number, n is the refractive index of the medium, τ_D is the radiative lifetime of the donor in the absence of the acceptor, and J_λ is the spectral overlap between the donor's photoluminescence spectrum and the acceptor's absorption spectrum [11]. The factor κ^2 accounts for the relative alignments of donor and acceptor dipoles, $\vec{\mu}_d$ and $\vec{\mu}_a$, with

$$\kappa = \cos(\theta_{da}) - 3\cos(\theta_{dr})\cos(\theta_{ar}) \tag{5.2}$$

Here, θ_{da} is the angle between the donor and acceptor dipoles and $\theta_{dr(ar)}$ is the angle between the donor (acceptor) dipole and the vector that is connecting the donor and acceptor ($\vec{r}$) as shown in the drawing of Fig. 5.1.

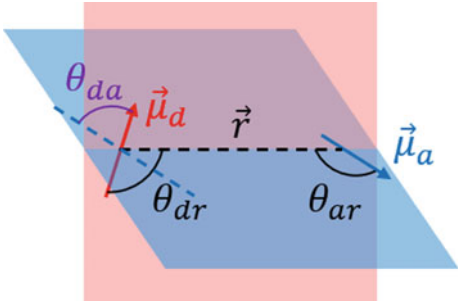

Fig. 5.1 Donor and acceptor dipoles $\vec{\mu}_d$ and $\vec{\mu}_a$ and the angles that determine their alignment factor, κ^2

Depending on the orientations of the donor and acceptor dipoles with respect to each other, κ^2 can take values ranging from 0 to 4. Typically, the fluorophores are randomly oriented and rotate freely in nonviscous solvents. When these rotations are much faster than the energy transfer, an average value for κ^2 is used. In the case of random 3D rotations of both, this average can be calculated as $\langle\kappa^2\rangle = 2/3$ [2].

Even though Eq. 5.1 indicates that the parameter that the rate of FRET most strongly depends on is the donor–acceptor separation, the effect of κ^2 is also significant as it can zero the rate of energy transfer. The effect of dipole orientation on FRET has been studied experimentally and theoretically on organic chromophores [12–14]. To analyze the orientation dependence of the energy transfer with colloidal NCs, we use a self-assembled monolayer of NPLs with a uniform orientation across the substrate. While colloidal quantum dots (QDs) have randomly oriented dipoles, which means that $\langle\kappa^2\rangle = 2/3$ in QD-to-QD FRET systems, $\langle\kappa^2\rangle$ can vary when anisotropic NCs such as nanorods and NPLs are employed. In addition, as NPLs cannot be approximated as pointlike particles, further modifications to the basic theory outlined in Eq. 5.1 is required.

To demonstrate that energy transfer can be tuned by controlling $\langle\kappa^2\rangle$ via setting the NPL orientation, we used an energy transfer working model with colloidal QDs as the donor and one monolayer of orientation-controlled NPLs as the acceptor. The monolayer of 4.5 ML CdSe NPLs on top of Al_2O_3-coated silicon substrates is deposited using the liquid interface self-assembly method described in Sect. 4.1 and also in [1]. The CdZnS/ZnS core/shell QDs are deposited directly on these self-assembled single NPL monolayers via spin coating. The schematic of this system is illustrated in Fig. 5.2a, b, along with the scanning electron microscopy images. The spectral overlap of the photoluminescence (PL) spectrum of the donor QDs and the absorption spectrum of the acceptor NPLs (Fig. 5.2c) implies that FRET from these QDs to the NPLs is possible when they are close. To calculate the rate of energy transfer, PL decays of the QD film in the presence, and the absence of the acceptor NPL monolayer have been collected. Compared to the PL decay of an only-QD sample, the PL decay of the QDs is significantly accelerated when they are on top of acceptor NPLs (Fig. 5.2d), which is due to the additional decay channel of FRET from the QDs to the NPLs. While the amplitude-averaged lifetime of the QD-only sample is 4.72 ns, it reduces to 1.08 ns for QDs on top of a face-down NPL monolayer and to 0.79 ns for QDs on a monolayer of edge-up NPLs.

The rate of nonradiative energy transfer from donor to acceptor can be experimentally calculated as

$$k_T = \frac{1}{\tau_{DA}} - \frac{1}{\tau_D} \tag{5.3}$$

where τ_D is the PL lifetime of the donor-only sample and τ_{DA} is the PL lifetime of the donor in the presence of acceptor(s). Using the measured PL lifetimes for the only-QD, QDs on face-down NPLs, and QDs on edge-up NPLs, the rate of FRET from QDs is then calculated as 0.71 ns^{-1} to the face-down NPL monolayer and 1.05 ns^{-1} to the edge-up NPL monolayer. These results show a ~50% enhancement

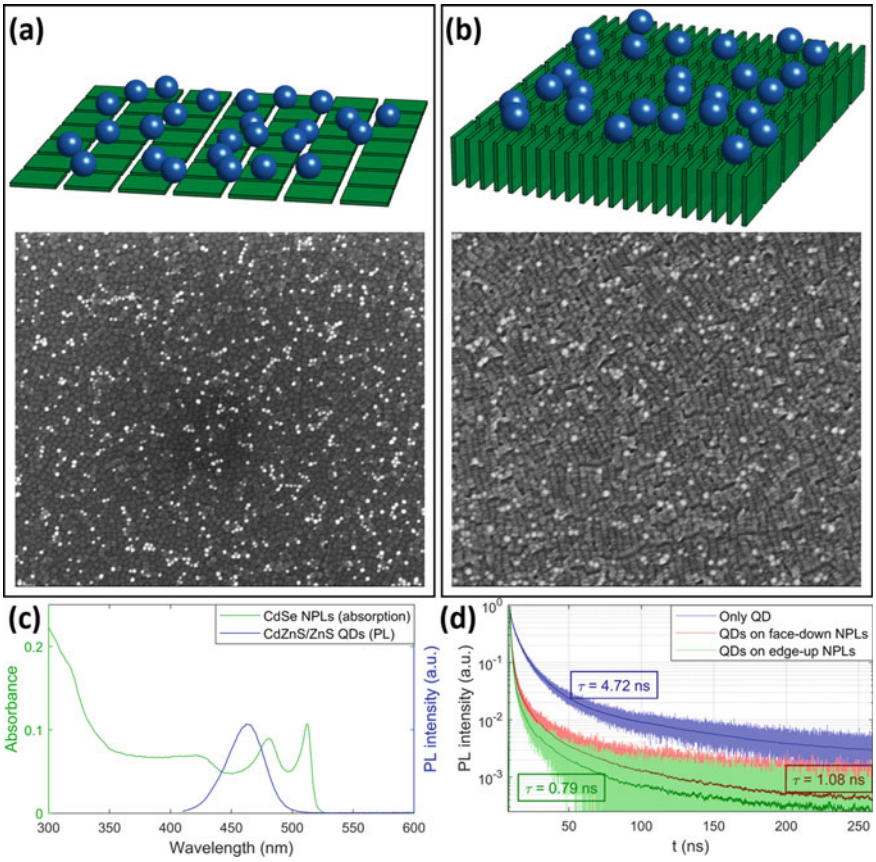

Fig. 5.2 Scanning electron microscopy images of spherical quantum dots (QDs) on top of a single monolayer of **a** face-down and **b** edge-up nanoplatelets (NPLs), along with the schematic drawings on top. **c** Absorbance spectrum of 4.5 ML CdSe NPLs (green) and photoluminescence (PL) spectrum of blue-emitting CdZnS/ZnS core/shell QDs. **d** Time-resolved PL decays of the only-QD sample (blue), QDs on top of face-down NPL monolayer (red), and on top of edge-up NPL monolayer (green), along with multiexponential fittings convolved with the instrument response function. Adapted with permission from [1]. Copyright 2019 American Chemical Society

in the energy transfer from the QDs to NPLs when the monolayer of NPLs is oriented vertically instead of horizontally.

A systematic study for distance dependence of FRET from QDs to an NPL monolayer has also been carried out in a similar configuration, which is shown in Fig. 5.3a, b. Herein, the QDs and the NPL monolayer are separated with a layer of Al_2O_3 spacer, which is coated on top of the self-assembled NPL monolayer via atomic layer deposition (ALD). PL decays for QDs deposited over a face-down and an edge-up NPL monolayer, separated by an Al_2O_3 spacer, are plotted in Fig. 5.3c and Fig. 5.3d, respectively. The PL decays of the no-spacer cases, presented in Fig. 5.2d, are also

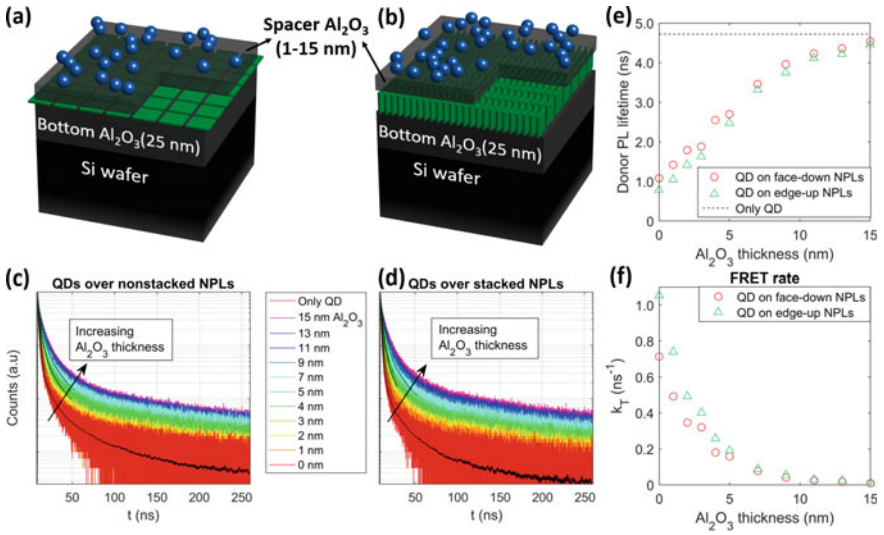

Fig. 5.3 FRET working model system between donor QDs and acceptor NPL monolayer for **a** face-down and **b** edge-up NPLs. PL decays of QDs over **c** face-down (nonstacked) and **d** edge-up (stacked) NPLs collected at the PL emission peak of the QDs (460 nm). The decays labeled as "0 nm" correspond to the PL decay without the spacer in between, which were separately plotted in Fig. 5.2d. **e** Amplitude-averaged PL decay lifetimes of QDs and **f** the FRET rates to the face-down (red circles) and edge-up NPLs (green triangles). The dashed line is the decay lifetime of the only-QD film. Adapted with permission from [1]. Copyright 2019 American Chemical Society

added here as a reference, labeled "0 nm" in the legend. The gradual acceleration of the PL decays with the decreasing spacer thickness is evident, which is due to the increase in FRET as the donor–acceptor distance gets smaller.

Similarly, the decays converge to that of only-QD as the thickness of the Al_2O_3 layer gets progressively larger. The amplitude-averaged lifetimes of these multiexponential decays are given in Fig. 5.3e. The rate of energy transfer versus spacer thickness, calculated using these lifetimes in Eq. 5.3, is plotted in Fig. 5.3f. The smaller decay lifetimes translate to higher FRET rates for QDs coupled with an edge-up NPL monolayer. It is also seen here that for any given separation, FRET from QDs to the edge-up NPL monolayer outpaces that to the face-down NPL monolayer.

5.1.1 Distance-Dependence of FRET from QDs to a Monolayer of NPLs

To quantify the distance dependence of the FRET from QDs to a monolayer of NPLs, the efficiency of FRET as a function of donor–acceptor distance can be analyzed. FRET efficiency is defined as the ratio of the FRET rate to the total rate of excitation decay. Following Eq. 5.3, it can be shown that FRET efficiency can be calculated as

$$\eta = 1 - \frac{\tau_{DA}}{\tau_D} \tag{5.4}$$

using the donor decay times that were experimentally obtained. The FRET efficiency can also be calculated theoretically using Eq. 5.1 as

$$\eta = \frac{1}{1 + (r/R_0)^6} \tag{5.5}$$

where

$$R_0 = \left(\frac{\kappa^2 \cdot 9 \ln 10}{128 \pi^5 N n^4} J_\lambda \right)^{1/6} \tag{5.6}$$

is the donor–acceptor distance for which the FRET efficiency is 50%, i.e. the rate of FRET equals that of radiative recombination at $r = R_0$. This distance is known as the Förster radius. r^{-6}-dependence of FRET means that FRET efficiency approaches unity below $r = R_0$ and quickly converges to zero for $r > R_0$. Therefore, the Förster radius is a useful metric to define the range of FRET However, r^{-6} dependence is valid only for pointlike donor and acceptor. To account for the multidimensional FRET systems where the distance dependence deviates from r^{-6}, Eq. 5.5 can be generalized as

$$\eta = \frac{1}{1 + (d/d_0)^p} \tag{5.7}$$

with d as the donor–acceptor separation and d_0 the Förster distance. While $p = 6$ for 0D donor and acceptor pairs, as stated above, it is expected to be smaller when the acceptor has higher dimensionality [15, 16].

In the case of a QD and an NPL monolayer, approximating the donor as point a dipole in the center of the QD, the donor–acceptor separation d is defined as the distance from the center of a QD to the top surface of the NPL monolayer (Fig. 5.4). This distance thus includes not only the Al_2O_3 thickness but also the length of the oleic acid ligands (1.8 nm) attached to NPLs and QDs, as well as the radius of the QDs (~4.5 nm). Fitting the efficiency versus distance to Eq. 5.7 results in $d_0 =$ 11.2 nm and $p = 3.78$ for FRET between QDs and face-down NPL monolayers, and $d_0 = 12.1$ nm and $p = 4.08$ for FRET between QD and edge-up NPL monolayers. For both NPL orientations, it is thus observed that the distance dependence is close to d^{-4}, as expected for the case of the plane of acceptors [15, 17].

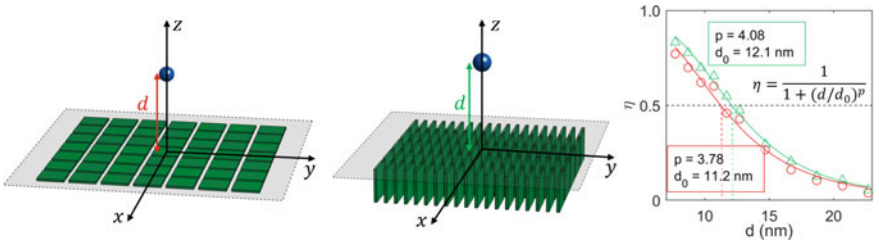

Fig. 5.4 Efficiency of FRET from QDs to a monolayer of face-down (red circles) and edge-up (green triangles) NPLs, as a function of QD to monolayer distance d. The distance is taken from the center of the quantum dot to the top of the NPL monolayer in both cases. Solid lines in the plot are fit to Eq. 5.7. The calculated efficiencies capture the d^{-4} behavior for face-down and edge-up NPL monolayer, with a Förster distance of 11.2 and 12.1 nm, respectively

5.1.2 *Theoretical Modeling of Orientation-Controlled FRET to NPLs*

Dipole alignment factor between QDs and oriented NPLs. The acceleration of FRET from QDs to a monolayer of NPLs when the NPLs are oriented vertically (edge-up) can be qualitatively accounted for from two aspects. The first one is that depositing NPLs vertically results in a denser packing of acceptors. Using the average lateral size of 14.4 nm, the thickness of 1.2 nm, and an approximate spacing of 3 nm in between the NPLs of a stack [18], the surface NPL density has been estimated as 3.1 $\times$ 10^3 and 1.3 $\times$ 10^4 NPLs/μm^2 for horizontally oriented (face-down) and vertically oriented (edge-up/stacked) NPLs, respectively [1]. As a result, more acceptor NPLs can be in close proximity to a QD when they are in edge-up orientation, which would increase the probability of energy transfer from the QD. Secondly, due to the in-plane confinement of the excitonic dipole in core NPLs [19, 20], the average dipole alignment factor $\langle \kappa^2 \rangle$ of a QD-NPL pair changes with NPL orientation. Considering a QD in the proximity of a 2D array of face-down NPLs, as seen in Fig. 5.5a, it can be shown that the average relative orientation factor of the QD dipole and an NPL dipole is [1]

$$\langle \kappa^2 \rangle = \frac{2 + 3sin^2\theta}{6} \tag{5.8}$$

where θ is the angle between the surface normal of the NPL plane and the distance vector $\overrightarrow{r}$ extending from the QD to the NPL dipole (Fig. 5.5a). Therefore, the degree of alignment of a freely rotating QD dipole and the in-plane confined NPL dipole also depends on the location of the NPL dipole with respect to the QD. Similarly, $\langle \kappa^2 \rangle$ can also be calculated with a 2D array of edge-up NPLs, such as the one in Fig. 5.5b. Here, the NPL stacks are assumed to be aligned with respect to each other, which is a reasonable approximation due to the local alignment of the stacks in the

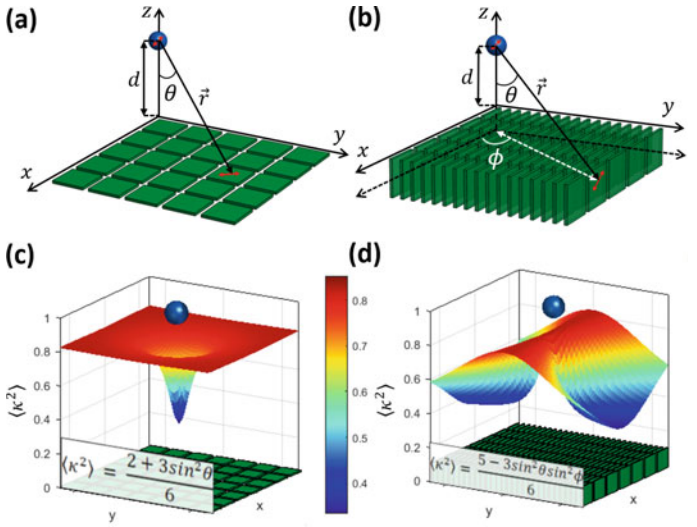

Fig. 5.5 **a**, **b** Relative alignment factor $\langle \kappa^2 \rangle$ of a QD dipole and an NPL dipole depends on the position of the NPL relative to the QD (determined by angles $\boldsymbol{\theta}$ and $\boldsymbol{\phi}$), as well as the NPL orientation. Plot of $\langle \kappa^2 \rangle$ as a function of NPL position for **c** face-down and **d** edge-up NPLs. Colorbar is common for **c** and **d**

edge-up NPL films across grains as large as a few μm [1]. In the configuration of Fig. 5.5b, the stacks are extended along the *y*-axis, in which case the NPL dipoles are confined into the *xz*-plane. It can then be shown that the dipole alignment factor, in this case, is [1]

$$\langle \kappa^2 \rangle = \frac{5 - 3\sin^2\theta \sin^2\phi}{6} \tag{5.9}$$

where ϕ is the angle between the x-axis and the projection of the distance vector onto the *xy*-plane. Similar to the face-down NPL case, $\langle \kappa^2 \rangle$ is strongly position-dependent. This position dependency of $\langle \kappa^2 \rangle$ is visualized in Fig. 5.5c and Fig. 5.5d for the case of face-down and edge-up NPL arrays, respectively.

Even though Eqs. 5.8 and 5.9 are valid everywhere across the acceptor plane, the value $\langle \kappa^2 \rangle$ is of the most interest only for the acceptor NPLs that are in the closest proximity of a donor QD, i.e. for θ close to zero, because regardless of $\langle \kappa^2 \rangle$, FRET to NPLs further away from the QD is highly unlikely due to the strong distance dependence. Setting, $\theta = 0$ in Eq. 5.8, one sees that $\langle \kappa^2 \rangle = 1/3$ for an NPL dipole that is positioned right below a QD. Similarly, Eq. 5.9 implies that $\langle \kappa^2 \rangle = 5/6$ at $\theta = 0$. This indicates that the dipole alignment of a QD and the NPLs right "below" that QD is strongly enhanced when the NPLs are standing vertically compared to a face-down NPL.

We, therefore, see that the enhancement of the FRET rate from QDs to NPLs when the NPLs adopt edge-up orientation could be explained by the change of the

NPL density and the dipole alignment factor for two different NPL orientations. The density of acceptors is larger in the case of edge-up orientation, and the donor–acceptor dipole coupling is stronger compared to the face-down NPLs due to larger $\langle\kappa^2\rangle$. Both of these factors favor the energy transfer to the edge-up NPLs more than to the face-down NPLs.

Delocalized dipole model. The energy transfer from the QDs to the NPL monolayers can be quantified using a model based on the Förster theory. Equation 5.1 holds for pointlike donors and acceptors, or more generally, when the size of the donor and acceptor is much smaller than the distance between them. In the case of this QD to NPL FRET system, QDs can be roughly approximated to have point dipoles since the excitonic wavefunction of this kind of CdZnS/ZnS core/shell QDs are mostly confined near the core [21]. However, as the lateral dimensions of the NPLs are comparable to the separation distances used, this approximation cannot be made with the NPLs. Instead, NPLs can be treated to have a point dipole state, whose wavefunction is assumed to be uniformly distributed across the lateral dimensions, neglecting the thickness. For the NPLs in the close proximity to a QD, the rate of FRET to a point dipole in the NPL can vary depending on the position of the dipole within the NPL. This is illustrated in Fig. 5.6 with face-down and edge-up NPLs. Depending on the exact position $\overrightarrow{r'}$ of the NPL dipole, the dipole–dipole distance $|\vec{r}| = \left|R_0 + \overrightarrow{r'}\right|$ also changes. This can be accounted for by calculating the FRET rate using Eq. 5.1 for a point dipole at any possible position $\overrightarrow{r'}$ across the lateral surface, and taking the average of these rates.

Considering a two-dimensional NPL grid such as the one depicted in Fig. 5.7, where each NPL is numbered by a set of two integers (q_x, q_y), the rate of FRET to a point dipole in an NPL with $(q_x, q_y) = (m, n)$ can be calculated using Eq. 5.1 as

$$k_{T,m,n|\overrightarrow{r'}} = \frac{\kappa_\theta^2}{\left|\vec{R}_{m,n} + \overrightarrow{r'}\right|^6 \tau_d} \frac{9ln10}{128\pi^5 N n^4} J_\lambda \tag{5.10}$$

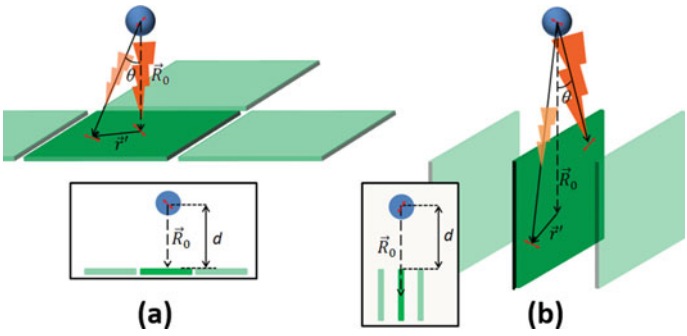

Fig. 5.6 Variation of dipole–dipole distance and its effect on the strength of FRET for a localized dipole state in **a** face-down and **b** edge-up NPLs. Insets show the cross-sections of the schematics

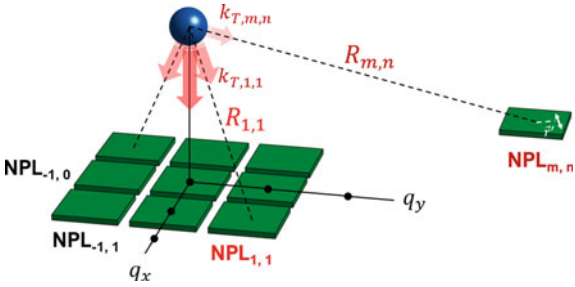

Fig. 5.7 The total rate k_T of FRET from a QD to an NPL monolayer is the sum of FRET rates to every NPL in the acceptor plane

where $\overrightarrow{R}_{m,n}$ is the vector from the QD donor to the center of NPL$_{m,n}$, $\overrightarrow{r'}$ is the position of the in-plane NPL dipole with respect to the center of the NPL. $\langle\kappa^2\rangle$ is calculated using Eq. 5.8 for the face-down NPL array and Eq. 5.9 for the edge-up NPL array. The rate of FRET to this NPL can then be found by

$$k_{T,m,n} = \frac{1}{A} \iint_{NPL_{m,n}} k_{T,m,n|\overrightarrow{r'}} dydx \tag{5.11}$$

where the A is the NPL lateral area and the integral is taken across the area occupied by NPL$_{m,n}$.

It should be noted that, in Eq. 5.10, $\langle\kappa^2\rangle$ is angle-dependent and changes with $\overrightarrow{r'}$. Therefore, $\langle\kappa^2\rangle$ is not the same everywhere across a single NPL, as also seen in Fig. 5.6. This variation in $\langle\kappa^2\rangle$ leads to significantly different results in calculating the FRET rate, especially in the proximity of the QD (i.e. for small m, n), and needs to be taken into account.

Finally, the FRET rate from the QD to all the NPLs can be found by

$$k_T = \sum_{q_x,q_y} k_{T,q_x q_y} \tag{5.12}$$

In the numerical calculations, the effective radiative recombination lifetime of donor-only QDs has been found by normalizing the measured amplitude averaged PL lifetime of 4.72 ns by the quantum efficiency of in-film QDs, which is measured as 65% [1], i.e. τ_d = 4.72 ns/0.65 = 7.26 ns. The refractive index is taken to be n = 1.72, which is close to the refractive index of Al_2O_3 as well as to the reported refractive indices of NC thin films [22, 23]. The separation between the NPLs in a two-dimensional grid has been taken as 3 nm. The thickness of the NPLs and the out-of-plane component of the excitonic dipole, which has been demonstrated to be tiny compared to the main in-plane component [19, 20], have been neglected.

The estimated rates of FRET from QDs to face-down and edge-up NPL monolayers using this model are plotted in Fig. 5.8a and Fig. 5.8b, respectively. It can be seen that the delocalized dipole approach based on the Förster theory can predict the energy transfer rates much better compared to the direct application of Förster's

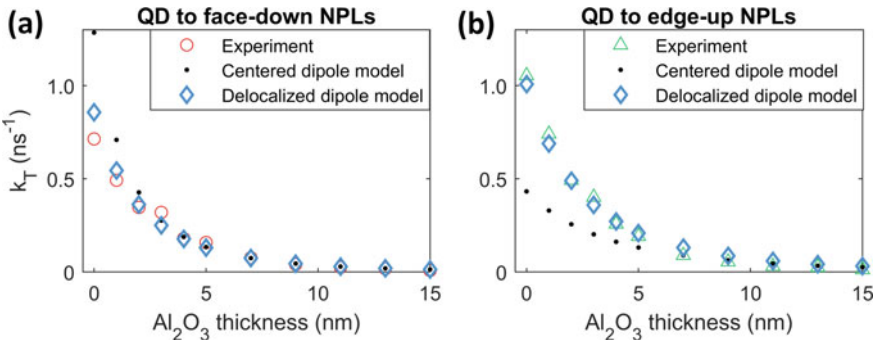

Fig. 5.8 Comparison of experimentally measured rates of FRET from QDs to a **a** face-down and **b** edge-up NPL monolayer, with the rates calculated theoretically using a center-to-center dipole approach (black dots) and a delocalized dipole approach (blue diamonds). Red circles in **a** and green triangles in **b** are the data presented in Fig. 5.3f. Adapted with permission from [1]. Copyright 2019 American Chemical Society

formula in Eq. 5.1 with an approximation of point dipole at the NPL center. In the case of the latter approach, the FRET rates divert significantly for the smaller spacer thicknesses. However, it is worth noting that the rate estimations using both approaches converge to the experimental values when the spacer thicknesses are larger. This can be expected as the centered point dipole approximation does hold for large enough donor–acceptor separations.

This work demonstrates the tunability of the nonradiative energy transfer with anisotropic colloidal NPLs by controlling the dipole alignment factor between a QD and NPLs. This control has been achieved through dictating the NPL orientation via liquid interface self-assembly deposition of CdSe NPLs as a single close-packed monolayer across cm^2-large areas. Being able to control the orientation of the NPLs this way enabled studying the anisotropy of NPLs on a macro-scale and shedding further light on the direction-dependent properties of colloidal semiconductor NPLs.

Readers interested in a more detailed overview and biological applications of FRET can refer to [11, 24–26]. For the fundamental theory of FRET, [2] and [27] can be consulted. More generalized theoretical treatments are available to tackle more complex FRET problems [14, 28–30]. For an overview of FRET with semiconductor NCs and its applications, readers are referred to [15, 31, 32].

5.2 Optically Active Planar Waveguides of Self-Assembled NPL Multilayers: Enabling Ultrathin Gain Media

Quasi-2D colloidal NPLs have rather favorable properties for optical gain, such as narrow photoluminescence due to the lack of inhomogeneous broadening [33] and much slower Auger recombination compared to quasi-0D colloidal QDs [34, 35].

Extensive studies on optical gain with NPLs have shown that NPLs are an excellent class of materials for lasing applications with reduced gain thresholds [22, 36, 37] and uncharacteristically high gain coefficients [38, 39]. NPLs of various compositions and heterostructures under different device geometries, including Fabry–Perot cavities [40], on-chip micropatterns [41, 42], whispering gallery mode [43, 44], and in-solution [45, 46] have been studied in terms of their amplified spontaneous emission (ASE) and lasing performance.

To evaluate the gain performance of the NC solids, NCs are typically prepared into thin films with a certain minimum thickness. The films are commonly prepared via spin-coating a concentrated NC solution or drop-casting onto the film. However, it is cumbersome to control the film thickness with these procedures. In addition, the film might also suffer from inhomogeneity and thickness variation [47–50], which is generally undesirable as it contributes to optical losses. Layer-by-layer assembly via dip coating can be used to obtain highly uniform and homogeneous NC films [51–53], yet this method requires the deposition of an oppositely charged layer of particles between the target NCs. The presence of such layers in between the nanoemitters reduces the particle density in the gain medium, which is undesirable in lasing.

To study the effect of film thickness on the optical gain of NPLs, we therefore deposit thin films of CdSe/$Cd_{0.25}Zn_{0.75}S$ core/shell NPLs using the multilayered liquid interface self-assembly deposition technique described in Sect. 4.2 and [54], by depositing one complete monolayer at a time, thereby achieving high precision in film thickness while maintaining large-scale film uniformity and tight packing of the deposited NPLs. These multilayered NPL films act as optically active two-dimensional waveguides, through which light can propagate and be amplified under sufficient pumping. The level of pumping required for optical amplification depends on several factors, including the presence of the waveguided optical modes, the electromagnetic confinement factor of these modes, the material gain coefficient of the NPLs, and the amount of losses due to external effects such as scattering. The self-assembled NPL multilayers facilitate studying and understanding the effect of optical confinement on the gain threshold owing to the precision in film thickness and uniformity and minimize the scattering losses due to ultralow roughness in films [54].

To quantify the ASE performance of NPL films having a different number of NPL monolayers, q, a stripe excitation geometry is used [55], which is schematically depicted in Fig. 5.9. A pulsed excitation beam with a pulse rate of 1 kHz and a pulse width of ~110 fs is focused into a stripe onto the sample using a cylindrical lens. The emission from this excited stripe of the film is collected into an optical fiber that is connected to an optical spectrometer. Using this setup, the optical gain performance of the multilayered NPL films with a number of layers ranging from $q = 1$ to $q = 15$ has been examined. An ASE feature in the PL spectrum has been detected for samples with $q \geq 6$, whereas only spontaneous emission has been observed for $q \leq 5$, even at high pump powers. The pump power-dependent PL spectra for multilayered NPL films of various thicknesses are plotted in Fig. 5.10a. ASE is evident from the emergence of a second, narrower emission feature beyond a threshold intensity, as well as the superlinear increase of the emission intensity with respect to the pump

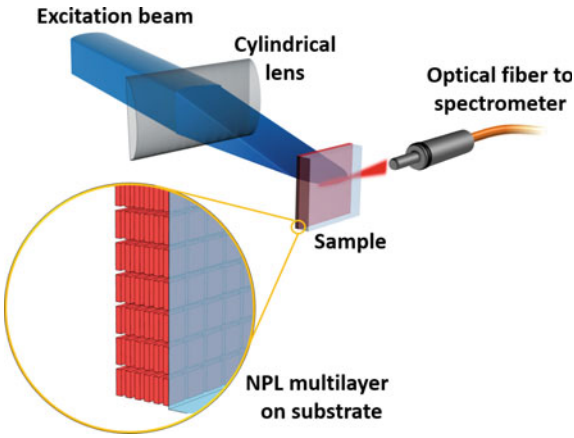

Fig. 5.9 Schematic of the optical setup for measuring amplified spontaneous emission (ASE). The pulsed excitation beam at 400 nm is focused onto the sample in one direction using a cylindrical lens. The emission of the excited slit is coupled into an optical spectrometer with the help of an optical fiber

fluence (Fig. 5.10b). The per-pulse gain thresholds have been determined to be 31.1, 19.3, and 7.5 μJ/cm^2 for $q = 6$, 9, and 15, respectively. The gain threshold is thus reduced significantly at the thickest sample in the set, with a thickness of 105 nm. The gradual drop of the threshold is also evident in Fig. 5.10c, where the gain thresholds for all 10 films with thicknesses from $q = 6$ to 15 monolayers.

Another notable observation is the evolution of the spectral position of the ASE peak with respect to the spontaneous emission peak for different q. While this shift is small for the thinnest slabs that are capable of displaying ASE ($q = 6$–8), the ASE feature shifts notably away from the spontaneous emission peak (Fig. 5.10d) for $q >$ 10. The difference between the two peaks is as large as 18 nm for the thickest NPL film [54]. A similar thickness-dependent ASE shift has been observed previously with organic-based 2D waveguides, and has been attributed to the change in the critical wavelength of propagation with film thickness, which enforces a blue shift in the ASE feature as the films get thinner [56–58]. In the case of the NPL superstructures, tuning the ASE peak across a 17-nm-wide spectral band (Table 5.1) is possible simply by adjusting the thickness of the NPL film at the monolayer precision.

To elaborate on the observed gain characteristics of these NPL films, numerical electromagnetic calculations are carried out for optical mode analysis of the structure. When the NPL thin film is approximated as a 2D homogeneous slab, the entire structure can be modeled as an asymmetric planar waveguide, as described in Fig. 5.11a. Accordingly, the NPL slab of refractive index $n_2 = 2.10$ is sandwiched between semi-infinite media of air and fused silica on both sides, with refractive indices $n_1 = 1.00$ and $n_3 = 1.45$, respectively. As n_2 is larger than n_1 and n_3, guided modes in which electromagnetic waves can propagate across the NPL slab through total internal reflection can be present in the structure, given that the slab has a minimum critical thickness. For the transverse electric (TE) field, this required thickness is given by [59].

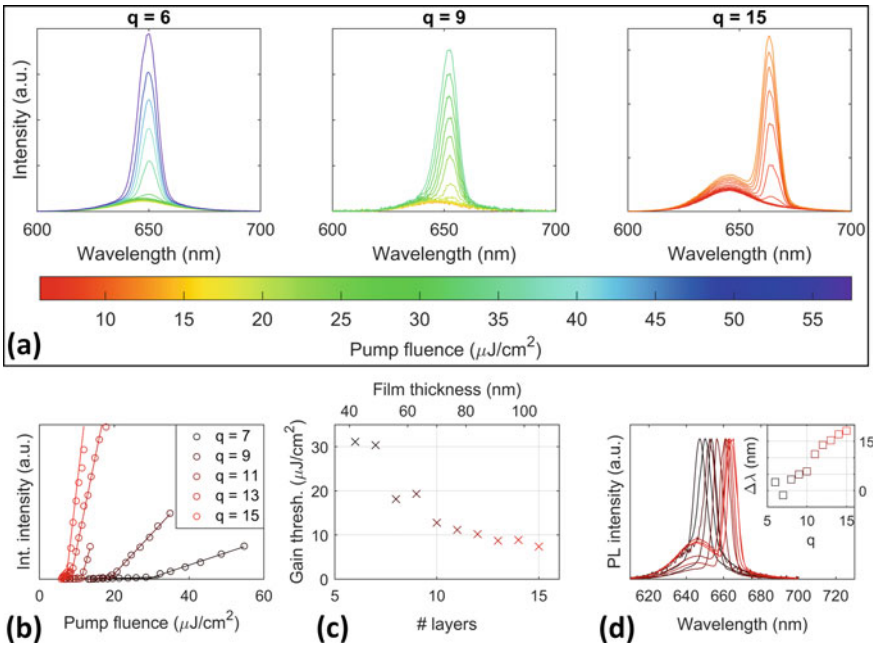

Fig. 5.10 **a** Emission spectra of NPL films having different number (q) of monolayers excited at different pump fluences: left, $q = 6$; center, $q = 9$; and right, $q = 15$. **b** Integrated intensity as a function of pump fluence for NPL films having a different number of multilayers. **c** Optical gain threshold of multilayered NPL films as a function of a number of NPL monolayers. **d** Shifting of the ASE peak with respect to the peak of the spontaneous emission feature for different q. Inset shows the difference between the ASE and spontaneous emission peaks as a function of the number of layers. Adapted with permission from [54]. Copyright 2020 American Chemical Society

Table 5.1 Gaussian fitting parameters for the spontaneous emission (SE) and amplified spontaneous emission (ASE) components of the PL spectra presented in Fig. 5.10d. The ASE spans a range of 17 nm from 6 to 15 monolayers. Reprinted with permission from [54]. Copyright 2020 American Chemical Society

# NPL layers (q)	SE peak (nm)	SE width (nm)	ASE peak (nm)	ASE width (nm)
6	647.6	31.8	650.2	7.2
7	648.8	32.6	647.4	7.4
8	650.3	29.1	653.7	5.9
9	647.8	30.3	652.7	7.6
10	651.3	35.0	657.1	6.2
11	649.7	35.5	660.8	5.9
12	648.0	34.0	661.9	5.7
13	647.7	32.3	663.0	5.5
14	647.7	33.0	664.8	5.5
15	645.9	31.1	664.1	7.2

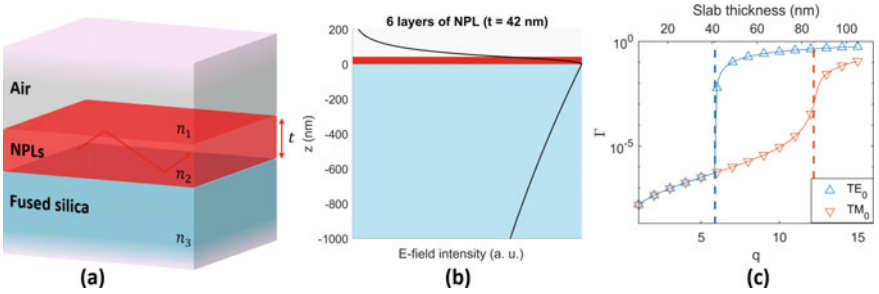

Fig. 5.11 Asymmetric planar waveguides of self-assembled NPL superstructures. **b** Electric field profile of the fundamental TE mode for the NPL slab with $q = 6$. Reprinted with permission from [54]. Copyright 2020 American Chemical Society. **c** Optical confinement factor Γ of TE_0 (solid blue line) and TM_0 (solid orange line) modes calculated at 650 nm as a function of slab thickness. Blue up triangles and orange down triangles mark the thickness of q-layered NPL films from $q = 1$ to $q = 15$. Blue and orange vertical dashed lines indicate the calculated critical thicknesses of 41.2 and 85.4 nm for the existence of TE_0 and TM_0 modes, respectively

$$t_c^{(TE)} = \frac{\lambda}{2\pi\sqrt{n_2^2 - n_3^2}}\left[m\pi + \tan^{-1}\left(\sqrt{\frac{n_3^2 - n_1^2}{n_2^2 - n_3^2}}\right)\right] \tag{5.13}$$

where m is the order of the electromagnetic mode that can take integer values starting from zero and λ the propagation wavelength. For the presence of the TM_m mode, the critical thickness is [59]

$$t_c^{(TM)} = \frac{\lambda}{2\pi\sqrt{n_2^2 - n_3^2}}\left[m\pi + \tan^{-1}\left(\frac{n_2^2}{n_1^2}\sqrt{\frac{n_3^2 - n_1^2}{n_2^2 - n_3^2}}\right)\right] \tag{5.14}$$

With $\lambda = 650$ nm, the critical thicknesses for the TE_0 and TM_0 modes are 41.2 nm and 85.4 nm, respectively. The critical thickness increases to 255 nm for the TE_1 mode and 299 nm for the TM_1 mode. Since the maximum thickness for this set of self-assembled NPL waveguides is 105 nm (see Sect. 4.2), $m = 1$ or higher order modes are not present in these waveguides, and TE_0 and TM_0 are the only modes that are relevant. Accordingly, the waveguiding starts at $q = 6$, which is barely thicker than $t_c^{(TE)}$, with only the TE_0 mode available. The mode profile for this sample is plotted in Fig. 5.11b. It can be seen that only a small fraction of the electromagnetic energy is confined within the NPL slab, while the rest is leaking out of the structure on both air and substrate sides. It is only this portion of the mode energy that propagates through the NPL slab and is capable of inducing light amplification. For an optical mode of the planar waveguide, this fraction of energy is called the mode confinement factor and can be quantified as [59]

$$\Gamma = \frac{Re\left\{\int_0^t \left(\vec{E} \times \vec{H}^*\right) \cdot \vec{z}\, dx\right\}}{Re\left\{\int_{-\infty}^{\infty} \left(\vec{E} \times \vec{H}^*\right) \cdot \vec{z}\, dx\right\}} \tag{5.15}$$

where $\vec{E}$ and $\vec{H}$ are the electric and magnetic field vectors, respectively, t is the NPL film thickness and the substrate-NPL boundary is at $z = 0$ so that the integral in the numerator is taken along the thickness of the NPL film. The mode confinement factor for the TE_0 and TM_0 modes in these NPL waveguides is plotted in Fig. 5.11c for 1–15-layered NPLs. It can be seen that the confinement factor Γ increases monotonically with the number of NPL layers q (i.e. film thickness). Γ of the TE_0 mode undergoes a significant jump of 4 orders of magnitude from $q = 5$ and $q = 6$ due to the onset of waveguiding. The confinement of the TM_0 field experiences a similar jump of 2 orders of magnitude when q increases from 12 to 13. In general, by increasing the thickness of the gain medium, the optical gain is facilitated by more efficient confinement of the electromagnetic energy within the NPL slab, which is in line with the decrease of the ASE threshold with increasing film thickness.

While there is only the TE_0 mode for the thinner NPL waveguides, the TM_0 mode also emerges beyond $t = t_c^{(TM)} = 85.4$ nm, i.e. for the samples $q = 13$–15. The effect of the emergence of this second guided mode can be understood via polarization-dependent ASE measurements. Considering the geometry in Fig. 5.12a, the polarization of the ASE signal propagating along the x-axis is expected to have an electric field in the y-direction for the TE field and in the z direction for the TM field. The angle-dependent ASE intensity measurements confirm the existence of the TM mode in the thickest NPL films by revealing that part of the ASE in these films is polarized along the z-axis. A comparison of the angle-dependent ASE intensity for an NPL waveguide that only allows TE_0 mode ($q = 11$) and another one where both TE_0 and TE_0 modes are present ($q = 15$) can be seen in Fig. 5.12b. The presence of the ASE signal at 90° polarization for the 15-layered sample confirms the emergence of TM_0 mode and emission. The degree of linear polarization is given as

$$V = \frac{I_{max} - I_{min}}{I_{max} + I_{min}} \tag{5.16}$$

where I_{max} and I_{min} are the maximum and minimum angle-dependent emission intensities. Fitting the polarized intensity data to $I(\theta) = a + b\cos^2\theta$, the polarization degree can be found as $V = b/(b + 2a)$. The polarization degree of the ASE from $q = 11$ sample is then calculated as $V = 0.97$, while $V = 0.60$ is found for $q = 15$. The evolution of linear polarization degree before and after the critical thickness $t_c^{(TM)} = 85.4$ nm is shown in Fig. 5.12c. The significant drop in the ASE polarization from $q = 12$ to $q = 13$ is evident, which is due to the emergence of the TM_0 mode and partial coupling of the guided ASE into this mode.

It should be noted that, even with the presence of an available TM mode, coupling into this TM mode requires dipole oscillations along a suitable direction. Figure 5.12a

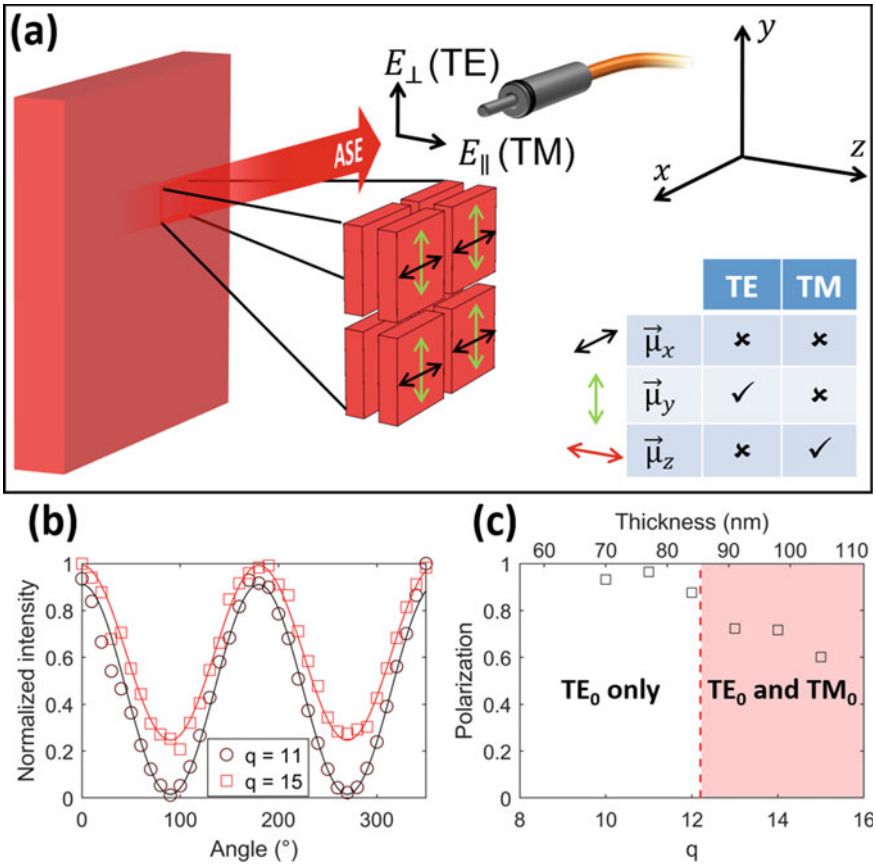

Fig. 5.12 **a** Polarization of the ASE of the thin NPL slab propagating along the *x*-axis. In this case, the TE field will be polarized in the y-direction, while the TM field will be polarized in the z-direction. Dipoles oscillating along the *y*- and *z*-axis can emit photons into TE and TM modes, respectively, while NPL dipoles oscillating along the *x*-direction will not couple to either of the waveguided modes. **b** ASE intensity as a function of polarizer angle for 11- and 15-layered NPL films. The polarizer angle of 0° (90°) corresponds to the TE (TM) polarization. **c** Degree of polarization as a function of the number of NPL layers in the film. The dashed red line indicates the critical thickness for TM_0 mode. **b**, **c** Adapted with permission from [54]. Copyright 2020 American Chemical Society

shows which components of an NPL emission dipole are capable of contributing to the guided mode emissions along the direction of ASE emission (selected as the *x*-axis in the figure). In this configuration, one of the in-plane NPL dipoles, $\vec{\mu}_y$, can have TE far-field radiation in the *x*-direction, while it cannot emit into the TM modes. The far-field emission of the other in-plane dipole, $\vec{\mu}_x$, on the other hand, cannot couple into either TE or TM modes in the *x*-direction. The only possible source of a TM electric field that propagates along the *x*-axis is a dipole oscillating along the *z*-direction, i.e. the out-of-plane component of an NPL emission dipole.

The results of these polarization experiments, therefore, prove that unlike core-only NPLs, for which the emission dipole is almost entirely confined within the NPL plane [19, 20], the core–shell NPLs may possess an out-of-plane component in their emission dipoles, possibly due to the leakage of the excitonic wavefunction into the shell. Therefore, in a multilayered planar waveguide constructed with face-down core-only NPLs having 4.5 or 5.5 ML thickness, this TM polarization in the ASE is not expected even if the NPL slab is thick enough to allow propagation of TM waves. In that case, the ASE is predicted to have virtually 100% linear polarization regardless of the number of face-down NPL monolayers.

5.2.1 Dielectric-Assisted Enhancement of the Optical Confinement in Self-Assembled NPL Waveguides

The six-layered NPL film that displays optical gain has enabled observation of optical gain from a film that has a mere 42 nm thickness for a gain medium on a bare substrate without optical feedback. Achieving optical gain from an even fewer number of NPL monolayers is possible when the presence of guided modes is ensured. To this end, a dielectric coating of TiO_2 with a high refractive index of 2.41 has been deposited onto the substrate via the atomic layer deposition technique before depositing the self-assembled monolayers of CdSe/CdZnS core/shell NPLs (Fig. 5.13a) [60]. Such stratified media of NC-dielectric composites enable the enhancement of the optical mode confinement around the NC layer [61]. In the case of TiO_2-supported NPL multilayers, numerical mode calculations revealed that for a three-layered NPL film, an optimum TiO_2 thickness of 55 nm is required to ensure the presence of the TE_0 mode in the waveguide structure and maximize its confinement factor across the NPL layer [60]. Owing to the TiO_2 layer under the NPL multilayers, the Γ-factor for the three-layered asymmetric waveguide is nearly as large as the Γ-factor of a six-layered film on a bare substrate (Fig. 5.13b). Thanks to this enhancement in the mode confinement, observing ASE has been possible from only a three-layer (21 nm) thick film of self-assembled NPLs [60]. Supporting the NPL film with a TiO_2 layer on both sides enables a more efficient mode confinement so that the NPL thickness can be reduced even further while maintaining the optical gain. With an NPL bilayer, electromagnetic simulations for mode analysis revealed that Γ is maximized when there is a 40 nm TiO_2 layer at the bottom and 50 nm TiO_2 on top (Fig. 5.13d, e) [60]. Similar to the asymmetric waveguide case, ASE is also observed from this symmetric waveguide (Fig. 5.13f), for which the thickness of the gain medium is only 14 nm.

Lasing action has also been demonstrated using ultrathin self-assembled NPL films inside Fabry–Perot cavities. Monolithic fabrication of vertical-cavity surface-emitting lasers (VCSELs) with distributed Bragg reflectors (DBR) as mirrors and a few monolayers of self-assembled NPLs in between them enables single-mode lasing with high-quality factor [62]. Herein, to achieve the spectral alignment between the peak of the NPL gain spectrum and the resonant modes of the cavity, a thin film of

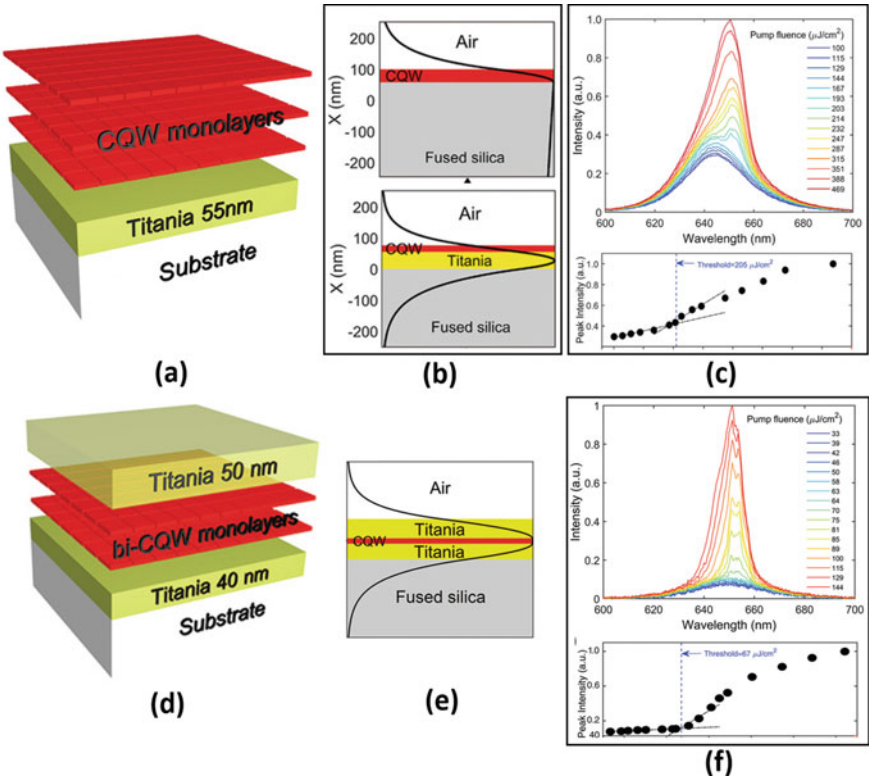

Fig. 5.13 **a** Schematic of asymmetric waveguide consisting of three monolayers of NPLs (i.e. CQWs) on top of a thin TiO_2 film and fused silica substrate. **b** The presence of the high-dielectric index TiO_2 layer enables the TE_0 mode and helps with more efficient optical mode confinement. **c** Pump-dependent emission spectra (top) and the peak intensity versus pump fluence (bottom) for the asymmetric waveguide structure. **d** Schematic, **e** mode profile, and **f** pump-dependent emission spectra of the planar waveguide made of an NPL bilayer sandwiched between slabs of TiO_2. Copyright 2020 Wiley. Used with permission from [60]. © 2020 Wiley–VCH GmbH

Al_2O_3, deposited via ALD, is employed inside the cavity (Fig. 5.14a, b). Another function of this thin Al_2O_3 layer is to ensure that the gain slab is positioned near the peak of the mode profile (Fig. 5.14b), thereby maximizing the stimulation of the gain medium by the highest possible electric field intensity across the cavity. For VCSELs with different NPL film thicknesses (1–4 monolayers), the Al_2O_3 layer thickness is optimized by numerical simulations on the resonance spectrum (Fig. 5.14c). In each case, the spectral position of the measured lasing peak shows an excellent agreement with the simulated ones (Fig. 5.14d). Lasing has been observed from all four VCSEL structures having 1–4 monolayers of NPLs with thresholds ranging from 78 to 112 $\mu J/cm^2$. The lasing threshold reduces monotonically with an increasing number of NPL layers. In each case, the lasing operation is single mode (Fig. 5.14e),

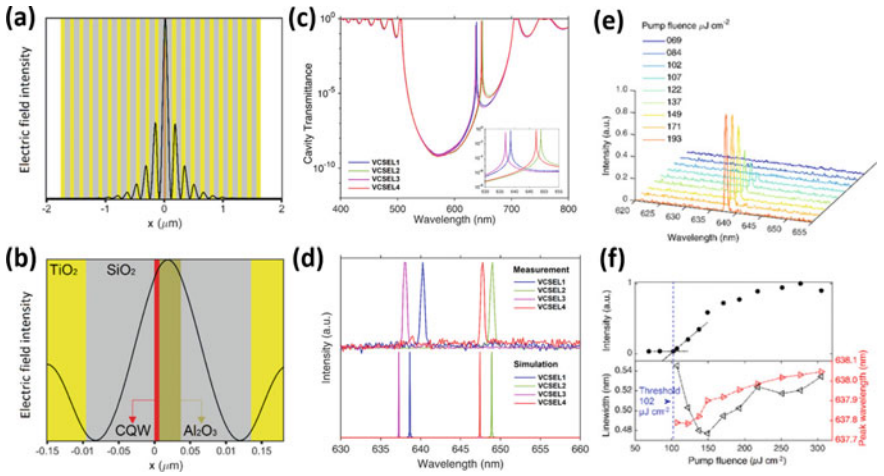

Fig. 5.14 **a** Electric field intensity profile of the resonant mode inside a DBR Fabry–Perot cavity with one monolayer of NPLs and 30 nm of Al_2O_3. **b** Magnified plot of the main lobe of the E-field intensity distribution in panel a. **c** Simulated transmission spectra for the proposed cavities having 1–4 NPL monolayers, in each case with a mode tuning Al_2O_3 layer with appropriate thickness. **d** Measured (top) and simulated (bottom) resonant modes in the VCSELs having 1–4 NPL monolayers. **e** Lasing spectra of the VCSEL having three monolayers of NPLs. **f** Intensity versus pump fluence for the measured lasing spectrum (top). Evolution of spectral linewidth and lasing wavelength with increasing pump fluence (bottom). Copyright 2021 Wiley. Used with permission from [62]. © 2021 Wiley–VCH GmbH

with a spectral linewidth of the lasing feature ranging from 0.46 to 0.8 nm [62] and quality factors as high as 1,400.

5.3 Other Applications for Liquid Interface NPL Assemblies: Photovoltaics, Displays, and Beyond

Besides being spectrally narrow and tunable emitters, colloidal NPLs are also efficient light absorbers owing to their large absorption cross-section. This property of NPLs can be used for transferring excitation into lesser absorbers through charge transfer or nonradiative energy transfer. Previously, colloidal QDs were employed to sensitize silicon for photovoltaic devices [63–65]. This approach aims to inject additional charges into the silicon layer via energy transfer from the NCs. This way, relatively weak absorption of silicon in the visible range due to its indirect bandgap can be compensated by additional excitonic energy that is fed by the NCs through a radiative or nonradiative energy transfer channel.

To study the prospects of silicon sensitization with colloidal NPLs, self-assembled monolayers of CdSe/CdZnS core/shell NPLs have been employed together with crystalline silicon, which forms a 2D donor/3D acceptor energy transfer working

model system [66]. To understand the FRET dynamics and its dependence on the donor–acceptor distance, the separation between the NPL monolayer and the silicon surface has been adjusted via a thin layer of Al_2O_3. The overall structure of this donor–acceptor energy transfer system is given in Fig. 5.15a. The time-resolved PL decays of the NPLs show the gradual acceleration of the PL decay of the NPLs (Fig. 5.15b), and shortening of their PL lifetimes (Fig. 5.15c), while the spacer thickness is decreased from 50 to 1 nm. The FRET rates calculated using Eq. 5.3 are plotted in Fig. 5.15d versus the separation between NPL donors and the surface of the silicon substrate. The logarithmic plot reveals the slope to be −1.02, suggesting an uncharacteristic d^{-1} dependence of FRET, which was attributed to the delocalization of the electric field across the NPL monolayer as well as inside silicon [66]. As a result of this d^{-1} dependence, the range of FRET can extend to a few tens of nm (Fig. 5.15e) despite the relatively small Förster distance of 6.1 nm [66].

To demonstrate the effect of the FRET from the NPL monolayer on the bulk silicon, a proof of concept photo-detecting device has been proposed and fabricated, which is schematically depicted in Fig. 5.15f. A silicon-on-insulator base is added Schottky contacts of aluminum, a spacer of Al_2O_3, and finally, a single monolayer of NPLs via liquid interface self-assembly. The photocurrent on the silicon slab has been observed to increase as much as threefold compared to the control sample with no NPL monolayer [66]. The enhancement factor is larger for smaller Al_2O_3 thicknesses (Fig. 5.15g) due to the acceleration of FRET from the NPLs to the silicon slab. This proof of concept device thus demonstrates the capability of a single NPL monolayer for silicon sensitization through FRET.

In the aforementioned reports, self-assembled NPLs have been used as continuous and large-scale films in the optoelectronic applications and systems in which they are employed. It is also of interest to create NC structures of smaller scale, such as NC micro- and nano-arrays, which can be utilized in applications including displays, waveguiding, and biosensing [67–69]. Such two-dimensional arrays of NCs or NC-organic hybrid systems have been created by deep direct patterning via electron beam lithography (EBL) [68, 70]. More recently, EBL has been employed in deep direct patterning of CdSe/$Cd_{0.25}Zn_{0.75}S$ NPL films to create on-chip self-resonant microlasers. This work reports deep patterning of 300 nm thick NPL films with high aspect ratio patterns and below 100 nm feature sizes [42].

EBL has also been utilized in the direct patterning of ultra-thin self-assembled NPL films. To this end, a sequential fabrication technique involving liquid interface NPL assembly and electron beam lithography has been proposed and demonstrated [71]. The fabrication steps of this approach are visualized in Fig. 5.16a–f. Initially, red-emitting CdSe/$Zn_yCd_{1-y}S$ core/shell NPLs are deposited onto the substrate via self-assembly on a dimethylformamide interface, resulting in two- or three-monolayered films with a face-down NPL orientation, corresponding to a film thickness of 7–12 nm [71]. This film thickness is adjusted by changing the concentration of the NPL solution.

After the EBL patterning of the red NPLs, green-emitting $CdSe_{1-x}S_x/Zn_yCd_{1-y}S$ are also deposited via the same-self-assembly procedure, followed by a second EBL process. The SEM images of patterned CdSe/$Zn_yCd_{1-y}S$ and $CdSe_{1-x}S_x/Zn_yCd_{1-y}S$

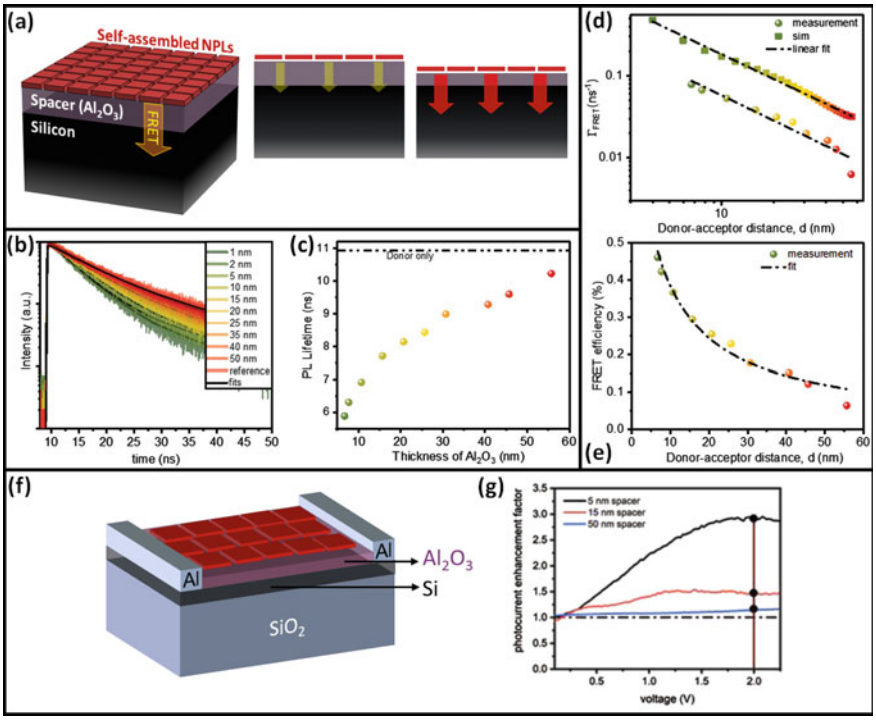

Fig. 5.15 **a** Energy transfer working model system from quasi-2D CdSe/CdZnS NPLs to 3D silicon, with Al_2O_3 as a spacer in between with controlled thickness. **b** Time-resolved PL decay and **c** amplitude-averaged PL lifetime of face-down the NPL monolayer on alumina-coated silicon and on quartz (donor-only reference sample). **d** Rate of FRET calculated using electromagnetic simulations (square markers) and calculated from the experimentally measured donor PL lifetimes (sphere markers). **e** FRET efficiency is calculated from the PL lifetimes. **f** Schematic of the proof-of-concept photodetector device to demonstrate photosensitization of silicon using a self-assembled NPL monolayer. **g** Photocurrent enhancement in the photodetector device with a monolayer of NPLs with respect to the negative control group device having no NPLs (dot-dashed line). **b**–**e**, **g** Copyright 2021 Wiley. Used with permission from [66]. © 2021 Wiley–VCH GmbH

NPLs are seen in Fig. 5.16g and Fig. 5.16h respectively. While the size of the square-shaped patterns here is ~250 nm, nanopatterns with the shape of hollow squares and circles and feature sizes of ~40 nm have also been demonstrated [71]. The fluorescence microscopy images of single-color 2D NPL arrays are given in Fig. 5.16i, j with patterns of 2 μm squares. This same square size has also been used in fabricating bicolor NPL arrays fabricated using sequential self-assembly and direct patterning steps, as seen in the SEM image of Fig. 5.16k and fluorescence microscopy image of Fig. 5.16l. The fluorescence intensity profile in Fig. 5.16m reveals that the photoluminescence intensity of each pixel remains constant for each color, suggesting that homogeneity is preserved after the patterning steps. Such pixelated structures of

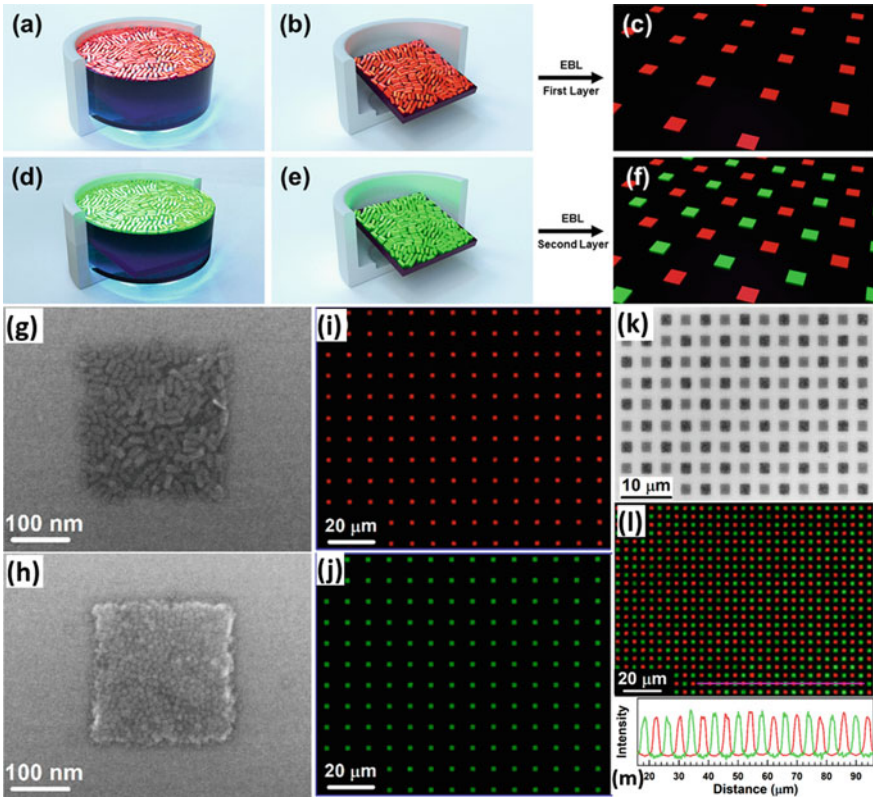

Fig. 5.16 **a**–**f** Fabrication of multicolored patterns via sequential self-assembly steps and direct electron beam lithography (EBL). High-resolution SEM images of self-assembled **g** red-emitting $CdSe/Zn_yCd_{1-y}S$ and **h** green-emitting $CdSe_{1-x}S_x/Zn_yCd_{1-y}S$ NPLs after direct patterning. Fluorescence microscopy images of red (**i**) and green (**j**) NPL arrays with 2 μm square patterns. **k** SEM and **l** fluorescence microscopy image of multicolored NPL patterns. **m** Light intensity profile of the patterned red and green NPLs across the pink line in panel **l**. Reprinted with permission from [71]. Copyright 2021 American Chemical Society

ultrathin NPL films can be beneficial for lighting and display applications, imaging systems, and on-chip microelectronics.

The studies presented in this chapter demonstrate how liquid interface self-assembly can help exploit the favorable optical properties of NPLs and their incorporation into optoelectronic devices and applications. The compatibility of this technique with other fabrication methods can facilitate this incorporation. The self-assembled thin films remaining intact after subsequent deposition steps or electron beam lithography [54, 71] are promising signs of compatibility.

Liquid interface self-assembly allows the deposition of device-scale uniform NPL films in a material-efficient manner. In this respect, it can be treated as a fabrication

tool such as thermal evaporation, chemical vapor deposition, or nanoimprint lithography, all of which are used for nanoscale device fabrication. In principle, many of the applications of NC optoelectronics, where other classes of NCs are employed, can benefit from the liquid air interface self-assembly. These applications extend to photodetection, field-effect transistors, solar cells, etc. In the case of applications of such as LEDs, liquid-air interface NPL assembly comes with the additional benefit of directional emission control. The layer-by-layer approach with liquid–air interface self-assembly can be highly beneficial in patterning NPL films of precise thickness in the ever-shrinking on-chip nanodevices.

References

1. Erdem O, Gungor K, Guzelturk B et al (2019) Orientation-controlled nonradiative energy transfer to colloidal nanoplatelets: engineering dipole orientation factor. Nano Lett 19:4297–4305
2. Förster T (1948) Zwischenmolekulare Energiewanderung und Fluoreszenz. Ann Phys 437:55–75
3. Stryer L, Haugland RP (1967) Energy transfer: a spectroscopic ruler. Proc Natl Acad Sci U S A 58:719–726
4. Steinberg IZ (1971) Long-range nonradiative transfer of electronic excitation energy in proteins and polypeptides. Annu Rev Biochem 40:83–114
5. Meadows D, Schultz JS (1988) Fiber-optic biosensors based on fluorescence energy transfer. Talanta 35:145–150
6. Walter NG (2001) Structural dynamics of catalytic RNA highlighted by fluorescence resonance energy transfer. Methods 25:19–30
7. Cho S, Jang J, Song C et al (2013) Simple super-resolution live-cell imaging based on diffusion-assisted Förster resonance energy transfer. Sci Rep 3:1208
8. Medintz IL, Clapp AR, Mattoussi H et al (2003) Self-assembled nanoscale biosensors based on quantum dot FRET donors. Nat Mater 2:630–638
9. Franzl T, Klar TA, Schietinger S et al (2004) Exciton recycling in graded gap nanocrystal structures. Nano Lett 4:1599–1603
10. Alivisatos AP, Gu W, Larabell C (2005) Quantum dots as cellular probes. Annu Rev Biomed Eng 7:55–76
11. Lakowicz JR (2006) Energy Transfer. Principles of fluorescence spectroscopy, 3rd edn. Springer, New York, pp 443–475
12. Haas E, Ephraim-Katchalski-Katzir SIZ (1978) Effect of the orientation of donor and acceptor on the probability of energy transfer involving electronic transitions of mixed polarization. Biochemistry 17:5064–5070
13. Srinivas G, Bagchi B (2001) Effect of orientational motion of mobile chromophores on the dynamics of Förster energy transfer in polymers. J Phys Chem B 105:9370–9374
14. Wong KF, Bagchi B, Rossky PJ (2004) Distance and orientation dependence of excitation transfer rates in conjugated systems: beyond the Förster theory. J Phys Chem A 108:5752–5763
15. Rogach AL, Klar TA, Lupton JM et al (2009) Energy transfer with semiconductor nanocrystals. J Mater Chem 19:1208
16. Hernández-Martínez PL, Govorov AO, Demir HV (2013) Generalized theory of Förster-type nonradiative energy transfer in nanostructures with mixed dimensionality. J Phys Chem C 117:10203–10212
17. Hernández-Martínez PL, Govorov AO, Demir HV (2014) Förster-Type nonradiative energy transfer for assemblies of arrayed nanostructures: confinement dimension vs stacking dimension. J Phys Chem C 118:4951–4958

18. Guzelturk B, Erdem O, Olutas M et al (2014) Stacking in colloidal nanoplatelets: tuning excitonic properties. ACS Nano 8:12524–12533
19. Scott R, Heckmann J, Prudnikau AV et al (2017) Directed emission of CdSe nanoplatelets originating from strongly anisotropic 2D electronic structure. Nat Nanotechnol 12:1155–1160
20. Gao Y, Weidman MC, Tisdale WA (2017) CdSe nanoplatelet films with controlled orientation of their transition dipole moment. Nano Lett 17:3837–3843
21. Lee KH, Lee JH, Song WS et al (2013) Highly efficient, color-pure, color-stable blue quantum dot light-emitting devices. ACS Nano 7:7295–7302
22. She C, Fedin I, Dolzhnikov DS et al (2014) Low-threshold stimulated emission using colloidal quantum wells. Nano Lett 14:2772–2777
23. Dement DB, Puri M, Ferry VE (2018) Determining the complex refractive index of neat CdSe/CdS quantum dot films. J Phys Chem C 122:21557–21568
24. Wu P, Brand L (1994) Resonance energy transfer: methods and applications. Anal Biochem 218:1–13
25. Clegg RM (1995) Fluorescence resonance energy transfer. Curr Opin Biotechnol 6:103–110
26. Selvin PR (2000) The renaissance of fluorescence resonance energy transfer. Nat Struct Biol 7:730–734
27. Kuhn H (1970) Classical aspects of energy transfer in molecular systems. J Chem Phys 53:101–108
28. Wolber PK, Hudson BS (1979) An analytic solution to the Förster energy transfer problem in two dimensions. Biophys J 28:197–210
29. Dewey TG, Hammes GG (1980) Calculation on fluorescence resonance energy transfer on surfaces. Biophys J 32:1023–1035
30. Hernández Martínez PL, Govorov A, Demir HV (2017) Understanding and modeling Förster-type resonance energy transfer (FRET) : FRET from single donor to single acceptor and assemblies of acceptors, vol 2, 1st edn. Springer Singapore
31. Guzelturk B, Demir HV (2016) Near-field energy transfer using nanoemitters for optoelectronics. Adv Funct Mater 26:8158–8177
32. Cardoso Dos Santos M, Algar WR, Medintz IL, Hildebrandt N (2020) Quantum dots for Förster resonance energy transfer (FRET). TrAC Trends Anal Chem 125:115819
33. Ithurria S, Tessier MD, Mahler B et al (2011) Colloidal nanoplatelets with two-dimensional electronic structure. Nat Mater 10:936–941
34. She C, Fedin I, Dolzhnikov DS et al (2015) Red, yellow, green, and blue amplified spontaneous emission and lasing using colloidal CdSe nanoplatelets. ACS Nano 9:9475–9485
35. Pelton M, Andrews JJ, Fedin I et al (2017) Nonmonotonic dependence of auger recombination rate on shell thickness for CdSe/CdS core/shell nanoplatelets. Nano Lett 17:6900–6906
36. Diroll BT, Talapin DV, Schaller RD (2017) Violet-to-blue gain and lasing from colloidal CdS nanoplatelets: low-threshold stimulated emission despite low photoluminescence quantum yield. ACS Photon 4:576–583
37. Delikanli S, Isik F, Shabani F et al (2021) Ultralow threshold optical gain enabled by quantum rings of inverted type-I CdS/CdSe core/crown nanoplatelets in the blue. Adv Opt Mater 9:2002220
38. Guzelturk B, Pelton M, Olutas M, Demir HV (2019) Giant modal gain coefficients in colloidal II-VI nanoplatelets. Nano Lett 19:277–282
39. Geiregat P, Tomar R, Chen K et al (2019) Thermodynamic equilibrium between excitons and excitonic molecules dictates optical gain in colloidal CdSe quantum wells. J Phys Chem Lett 10:3637–3644
40. Guzelturk B, Kelestemur Y, Olutas M et al (2014) Amplified spontaneous emission and lasing in colloidal nanoplatelets. ACS Nano 8:6599–6605
41. Yang Z, Pelton M, Fedin I et al (2017) A room temperature continuous-wave nanolaser using colloidal quantum wells. Nat Commun 8:143
42. Gheshlaghi N, Foroutan-Barenji S, Erdem O et al (2021) Self-resonant microlasers of colloidal quantum wells constructed by direct deep patterning. Nano Lett 21:4598–4605

43. Sak M, Taghipour N, Delikanli S et al (2020) coreless fiber-based whispering-gallery-mode assisted lasing from colloidal quantum well solids. Adv Funct Mater 30:1907417
44. Duan R, Zhang Z, Xiao L et al (2022) Ultralow-threshold and high-quality whispering-gallery-mode lasing from colloidal core/hybrid-shell quantum wells. Adv Mater 34:2108884
45. Li M, Zhi M, Zhu H et al (2015) Ultralow-threshold multiphoton-pumped lasing from colloidal nanoplatelets in solution. Nat Commun 6:8513
46. Maskoun J, Gheshlaghi N, Isik F et al (2021) Optical microfluidic waveguides and solution lasers of colloidal semiconductor quantum wells. Adv Mater 33:2007131
47. Bornside DE, Macosko CW, Scriven LE (1987) Modeling of spin coating. J Imaging Sci Technol 13:122–130
48. Hall DB, Underhill P, Torkelson JM (1998) Spin coating of thin and ultrahin polymer films. Polym Eng Sci 38:2039–2045
49. Malynych S, Luzinov I, Chumanov G (2002) Poly(vinyl pyridine) as a universal surface modifier for immobilization of nanoparticles. J Phys Chem B 106:1280–1285
50. Arscott S (2020) The limits of edge bead planarization and surface levelling in spin-coated liquid films. J Micromechanics Microengineering 30:025003
51. Lin YW, Tseng WL, Chang HT (2006) Using a layer-by-layer assembly technique to fabricate multicolored-light-emitting films of CdSe@CdS and CdTe quantum dots. Adv Mater 18:1381–1386
52. Roither J, Pichler S, Kovalenko MV et al (2006) Two- and one-dimensional light propagations and gain in layer-by-layer-deposited colloidal nanocrystal waveguides. Appl Phys Lett 89:111120
53. Suarez I, Munoz R, Chirvony V et al (2017) Multilayers of CdSe/CdS/ZnCdS core/wings/shell nanoplatelets integrated in a polymer waveguide. IEEE J Sel Top Quantum Electron 23:1–8
54. Erdem O, Foroutan S, Gheshlaghi N et al (2020) Thickness-tunable self-assembled colloidal nanoplatelet films enable ultrathin optical gain media. Nano Lett 20:6459–6465
55. Shaklee KL, Nahory RE, Leheny RF (1973) Optical gain in semiconductors. J Lumin 7:284–309
56. Sheridan AK, Turnbull GA, Safonov AN, Samuel IDW (2000) Tuneability of amplified spontaneous emission through control of the waveguide-mode structure in conjugated polymer films. Phys Rev B Condens Matter Mater Phys 62:929–932
57. Peng X, Liu L, Wu J et al (2000) Wide-range amplified spontaneous emission wavelength tuning in a solid-state dye waveguide. Opt Lett 25:314
58. Calzado EM, Villalvilla JM, Boj PG et al (2005) Tuneability of amplified spontaneous emission through control of the thickness in organic-based waveguides. J Appl Phys 97:093103
59. Yariv A, Yeh P (2007) Photonics: optical electronics in modern communications. Oxford University Press, New York, NY, USA
60. Foroutan-Barenji S, Erdem O, Gheshlaghi N et al (2020) Optical gain in ultrathin self-assembled bi-layers of colloidal quantum wells enabled by the mode confinement in their high-index dielectric waveguides. Small 16:2004304
61. Xie W, Stöferle T, Rainò G et al (2017) On-chip integrated quantum-dot–silicon-nitride microdisk lasers. Adv Mater 29:2–7
62. Foroutan-Barenji S, Erdem O, Delikanli S et al (2021) Single-mode lasing from a single 7 nm thick monolayer of colloidal quantum wells in a monolithic microcavity. Laser Photonics Rev 15:2000479
63. Nguyen HM, Seitz O, Aureau D et al (2011) Spectroscopic evidence for nonradiative energy transfer between colloidal CdSe/ZnS nanocrystals and functionalized silicon substrates. Appl Phys Lett 98:161904
64. Nguyen HM, Seitz O, Peng W et al (2012) Efficient radiative and nonradiative energy transfer from proximal CdSe/ZnS nanocrystals into silicon nanomembranes. ACS Nano 6:5574–5582
65. Yeltik A, Guzelturk B, Hernandez-Martinez PL et al (2013) Phonon-assisted exciton transfer into silicon using nanoemitters: the role of phonons and temperature effects in Förster resonance energy transfer. ACS Nano 7:10492–10501
66. Humayun MH, Hernandez-Martinez PL, Gheshlaghi N et al (2021) Near-field energy transfer into silicon inversely proportional to distance using quasi-2D colloidal quantum well donors. Small 17:2103524

67. Kim T-H, Cho K-S, Lee EK et al (2011) Full-colour quantum dot displays fabricated by transfer printing. Nat Photonics 5:176–182
68. Palankar R, Medvedev N, Rong A, Delcea M (2013) Fabrication of quantum dot microarrays using electron beam lithography for applications in analyte sensing and cellular dynamics. ACS Nano 7:4617–4628
69. Prins F, Kim DK, Cui J et al (2017) Direct patterning of colloidal quantum-dot thin films for enhanced and spectrally selective out-coupling of emission. Nano Lett 17:1319–1325
70. Nandwana V, Subramani C, Yeh YC et al (2011) Direct patterning of quantum dot nanostructures via electron beam lithography. J Mater Chem 21:16859–16862
71. Samadi Khoshkhoo M, Prudnikau A, Chashmejahanbin MR et al (2021) Multicolor patterning of 2D semiconductor nanoplatelets. ACS Nano 15:17623–17634